Q2 # Optimization of figure of merit in label-free biochemical sensors by designing a ring defect coupled resonator

Lijun Huang [a,b], Huiping Tian [a,*], Daquan Yang [a,c], Jian Zhou [a], Qi Liu [a], Pan Zhang [a],
Q1 Yuefeng Ji [a]

[a] State Key Laboratory of Information Photonics and Optical Communications, School of Information and Communication Engineering,
Beijing University of Posts and Telecommunications, Beijing 100876, China
[b] Department of Physics and Information Engineering, Huaihua University, Hunan, Huaihua 418008, China
[c] School of Engineering and Applied Sciences, Harvard University, Cambridge, MA 02138, USA

A R T I C L E I N F O

A B S T R A C T

We propose a high figure of merit (FOM) biochemical sensor by designing a ring defect coupled resonator (RDCR) based on photonic crystal (PhC) slab. The design consists of ring resonant cavity which is coupled in and out with ring and line defect PhC structure. By a three dimensional finite-different time-domain (3D-FDTD) method, we demonstrate that the quality (Q) factor is greatly enhanced by altering the radius of air holes inner the ring resonant cavity and adjusting the width of line defect waveguide. In this paper, we obtain a highest Q up to 10^7 through numerical calculations. Even though water absorption at telecom wavelength range and random roughness of fabrication is considered, a Q of $\sim 33,517$ can be achieved. Simultaneously the proposed sensor possesses sensitivity (S) of 330 nm/RIU (refractive index unit), resulting in FOM of ~ 8000. Moreover, a minimal detection limit (DL) is obtained as good as 1.24×10^{-5}. Therefore, these suggest that this design is a promising candidate for label-free biochemical sensing in medical diagnosis, life science and environmental monitoring.

© 2014 Published by Elsevier B.V.

1. Introduction

In the past few decades, due to the robust characteristics such as ultracompact size, high sensitivity, accurate detection limit and easily integrated, optical refractive index (RI) sensors are widely researched for a large number of applications and dominant among the commercial landscapes of current sensing technologies. So far, optical RI sensors include surface plasmon resonance (SPR) sensors [1–3], long-period fiber grating (LPFG) sensors [4,5], ring resonators [6–13], micro-tube [14–16] and photonic crystal structure sensors [17–31]. A large number of sensors are used as biochemical sensors [3,6–17,19,21,24,27–29]. In these sensors, optical resonance peaks can be easily observed. That is, a change in RI around the region probed by resonant mode causes a relevant wavelength shift of optical sensor, and this change in resonant wavelength is converted to the sensing signal.

As shown in Table 1, micro-tube resonator sensors [14–16] and PhC-based sensors [17–26] have overall larger Q factor and sensitivity. The Q-factors of most PhC geometries are of 10^3–10^4 and the S's are around 100–1500 nm/RIU at around 1550 nm

wavelength, resulting in figure of merit ($FOM=S \cdot Q/\lambda_0$) are of 100–5000, where S, Q and λ_0 represent the sensitivity, quality factor and resonant wavelength, respectively. For example, Dorfner et al. [21] presented the design of L3 nanocavity coupled to photonic crystal waveguide for optical biosensor where Q factor of 6788 and S of 104 nm/RIU were obtained. Wang et al. [25] demonstrated S of 900 nm/RIU in slot double-beam cavities, whereas the Q factor was limited to 700. Yang et al. [26] demonstrated a nano-slotted parallel multibeam cavity which possesses S exceeding 800 nm/RIU and Q exceeding 10^7. Taking water absorption into consideration at telecom wavelength range, the Q of the sensor is limited to 10^4, resulting in FOM of ~ 5000. In order to enhance the FOM, we must increase the product of S and Q. However, the trade-off between S and Q limits FOM; we can make the optical mode more localized in the waveguide medium to achieve enough high quality factors, but simultaneously we must make the optical mode overlap strongly with the detecting target to obtain high sensitivity.

In this paper, we propose a novel paradigm employing photonic crystal ring defect coupled resonator (RDCR) for medical diagnosis and life science. We make optical mode more localized to obtain high Q by adjusting the radius of air hole and the width of waveguide. Simultaneously, we also make optical mode overlap strongly with the detecting target to enhance sensitivity. The

---

* Corresponding author.
    E-mail addresses: hptian@bupt.edu.cn (H. Tian), jyf@bupt.edu.cn (Y. Ji).

Table 1
Q factor, S, and FOM of Various Optical Index Sensors.

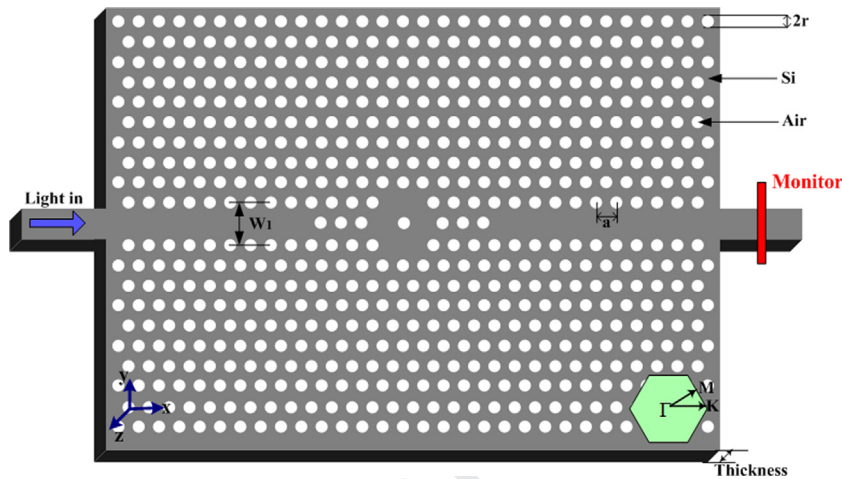| Sensing structure		Ref.	Q factor in water (At Telecom Range)	Sensitivity (nm/RIU)	FOM
SPR	Gold mushrooms	[3]	200	1015	108
Whispering-gallery mode(WGM) based	Microring	[6–13]	10^3–10^4	70–200	45–142
	Micro-tube	[14–16]	10^2–10^4	100–1100	55–8000
PhPhC based	1D nanobeam	[17]	$\sim 10^4$	~ 100	~ 645
	2D slab	[18–22]	10^3–10^4	100–300	200–645
	PhC slot	[23–26]	$\sim 10^4$	490–1500	300–5000

Fig. 1. 3D illustration of the initial ring defect coupled resonator, where a=348 nm, r=0.34a, T=0.55a, $W_1 = \sqrt{3}a$.

extensive simulation results demonstrate that the RDCR can possess high Q up to 10^7 in air medium when r_c and W equal to $0.40a$ and $0.985W_1$, respectively. Even if we consider the absorption of water and random roughness of fabrication at telecom wavelength range in simulation, a Q factor up to 33,517 can be obtained. We alter refractive index with n=1.315, 1.330 and 1.345, corresponding to deuterium water ($n_{1.330}$) and glycerol solutions ($n_{1.345}$), and the sensitivity S of 330 nm/RIU is calculated, resulting in FOM of ~ 8000. This is, to the best of our knowledge, the first geometry photonic crystal sensor structure that can lead to high FOM.

2. Ring defect coupled resonator design

The schematic diagram of the initial RDCR based on ring and line defect PhC slab structure is shown in Fig. 1. Compared with the pillar-array based PhC [22], the structure employs triangular lattice, hole-array PhC slab with large enough photonic band-gap (PBG) and small vertical loss (Fig. 1). In this paper, triangular lattice air holes are arranged in a silicon slab (n_{si}=3.48), where part of air holes is removed in order to form a ring and line defect waveguide. We simulate the RDCR structure by using the open source 3D-FDTD software Meep. In the simulation process, light source is placed at the head of the input line defect waveguide and monitor is placed at the end of the output line waveguide. We obtain the transmittance spectra through dividing the output power detected with the monitor by the input power of the source. We set resolution to 20 (that is, with a grid spacing of a/20, where a represents the lattice constant). The TE Gaussian-pulse source is used and run for several iterations. One-spatial unit thick perfectly matched layer (PML) which surrounds the simulation area absorbs the fields leaving the simulation region to implement reflections.

As shown in Fig. 1, the lattice constant a equals to 348 nm and the holes radius r is 0.34a (118 nm). The slab thickness, denoted as T and realized on silicon slab waveguide, equals to 0.55a (191 nm). Fig. 1 shows detailed design about the structure parameters including lattice constant, radius of holes, and thickness of PhC slab. The simulation results of the light propagation through the initial RDCR are showed in Fig. 2, in which we can find that the leakage of light is suppressed in out-plane direction (vertically) and the TE-like polarized light is coupled into the ring waveguide in-plane direction (horizontally). Fig. 3 shows the transmission spectra of initial RDCR and perfect PhC. As can be seen in Fig. 3, the effective working frequency of guided mode with the PBG is between 0.213($2\pi c/a$) and 0.313 ($2\pi c/a$), which is sufficiently wide for the sensor design. In initial RDCR design, the results show several different resonant modes at normalized frequency of 0.2261($2\pi c/a$), 0.2311($2\pi c/a$), 0.2646($2\pi c/a$), 0.3043($2\pi c/a$), and 0.3075($2\pi c/a$), which correspond to resonant wavelengths of 1816.67 nm, 1777.36 nm, 1552.34 nm, 1349.82 nm, 1335.75nm, respectively. We choose the resonant frequency of 0.2646($2\pi c/a$) to observe the shift of resonant wavelength when the structure and the refractive index are altered, respectively. By numerical calculations, the Q factor of resonant frequency 0.2646 ($2\pi c/a$) surrounded by red dashed equals to 6.02×10^6.

The Q factor of a cavity is determined by the energy loss per cycle versus the energy stored. The energy loss includes mainly reflection loss and the absorption loss of cavity material. Therefore, to improve the Q factor of the RDCR design, we should minimize the energy loss. With the RDCR structure, the corresponding Q factor can be given by [18,32]:

$$\frac{1}{Q} = \frac{1}{Q_{couple}} + \frac{1}{Q_{loss}} \tag{1}$$

where Q_{couple} represents the lifetime, that is, light can decay from the cavity into the waveguide, and Q_{loss} refers to materials
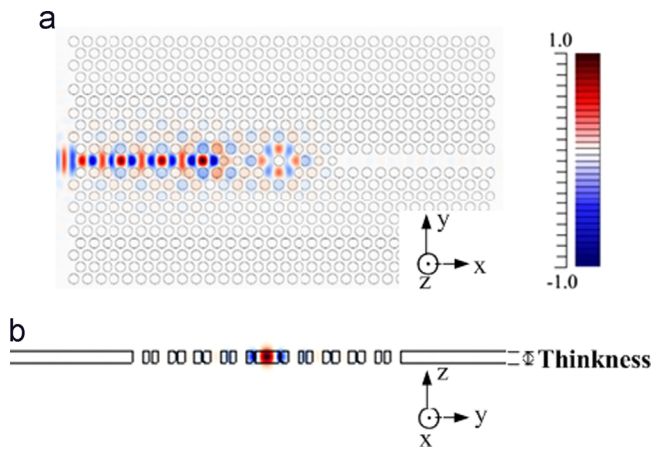
Fig. 2. Steady-state electric field profile for the fundamental TE mode propagates through the initial RDCR in (a) the *x–y* plane; (b) the *y–z* plane.
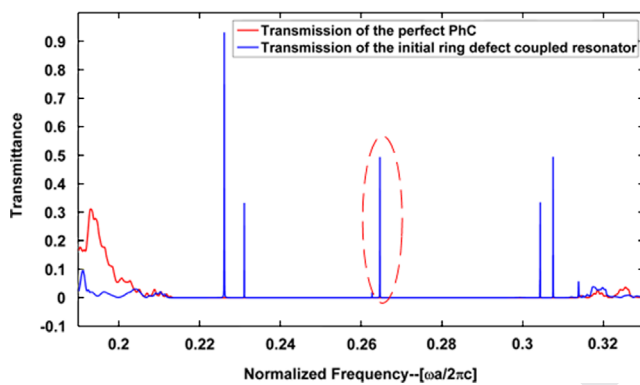

Q4 **Fig. 3.** The red line represents the transmission of perfect PhC and the blue line is the transmission of initial RDCR. To observe the shift of resonant frequency of $0.2646(2\pi c/a)$ surrounded by red dashed line when structure and RI are changed. (For interpretation of the references to color in this figure legend, the reader is referred to the web version of this article.)

absorption and radiation loss from the cavity into the surrounding air. We here alter the radius of air hole in the center of ring resonator and the width of line defect waveguide to decrease Q_{loss}, namely, we make the optical mode more localized in the waveguide medium so that higher Q factor can be obtained.

3. Ultra-high Q factor design in ring defect coupled resonator

In this paper, the Q-factor is enhanced by using heterostructure ring cavity [32–35] which is further designed by two routes: one is that altering the radius r_c of red holes in ring resonator, and the other one is that adjusting the width W of line defect waveguide. The detail of the RDCR structure is shown in Fig. 4. The theoretical results of 3D-FDTD simulation showing resonant frequencies and Q factors as a function of r_c are shown in Fig. 5(a). The transmission spectra of TE-like polarized lightwave with different parameters $r_c=0.34a$, $0.40a$ and $0.45a$ are shown in Fig. 6. In Fig. 5(a), we adjust the red air holes radius from $0.24a$ to $0.60a$ to optimize the Q factor. In the process of adjusting the red air holes, we find that the maximum Q factor of 6.93×10^6 is achieved when r_c equals to $0.40a$ and resonance frequency ω is $0.2672(2\pi c/a)$, and resonance frequency is pushed to higher frequency, due to the decrease in high-dielectric material and the increase in low-dielectric material in the cavity region. Moreover, although the coupling strength between ring resonant cavity and line defect waveguide is strong enough, namely, we obtain sufficiently high Q factor, there is a

limitation when r_c is adjusted from $0.24a$ to $0.60a$. That is because photons confined in ring resonant cavity is not enough and the lifetime of photons is not enhanced enough.

In view of the problems above, the line defect width W is locally modulated by shifting the position of blue air holes towards the inside (outside) from $0.92W_1$ to $1.01W_1$. This shift modulates the line defect cutoff frequency and creates the light confinement. Fig. 5(b) shows the resonant frequency and the Q factor as a function of the waveguide width W from $0.92W_1$ to $1.01W_1$ when $r_c=0.40a$. As seen, the optimized Q factor of 1.86×10^7 is calculated when $W=0.985W_1$. The simulation of electric field profile for the fundamental quasi-TE mode in $x–y$ plane and in $y–z$ plane, and output transmission spectrum of TE-like polarized profile lightwave in RDCR are plotted in Fig. 7 when $r_c=0.40a$, $W=0.985W_1$, respectively, by employing 3D-FDTD simulation based on structure design in Fig. 4. The inset shows that photons are confined strongly in both in-plane direction (horizontally) and out-plane direction (vertically). Therefore, the leakage of light becomes very small and the lifetime of photons is largely enhanced in this situation.

4. Sensitivity discussion for RDCR structure

4.1. Theory analysis

For the ring defect coupled resonator in Fig. 8, the detection of the bulk RI change mainly relies on light density in the core of ring resonant cavity. Therefore, increasing the fraction of light energy in the core can enhance sensitivity. The resonant wavelength, λ, is given by [10]:

$$2\pi R \cdot [n_1\eta_1 + n_3\eta_3 + n_2(1-\eta_1-\eta_3)] \approx l \cdot \lambda \qquad (2)$$

where l is an integer related to angular momentum, η_3 and η_1 are the fractions of light energy in core and surrounding mediums, and R is the effective inner radius of ring resonator. The dimensions of wavelength shift are dependent on the change of effective index of bound targets, namely, a change in RI, Δn, induces a wavelength shift $\Delta\lambda$ is given by:

$$\Delta\lambda \approx \frac{2\pi R}{L} \cdot \eta_3 \cdot \Delta n \approx \frac{\lambda}{n_2} \cdot \eta_3 \cdot \Delta n \qquad (3)$$

Considering the predominant fraction of light confined in ring resonator, we here used $L=2\pi n_2 R/\lambda$ and ignored the redistribution of light in core and surrounding environment. Where η_3 represents electric field decays exponentially in core and can be calculated as:

$$\eta_3 = \frac{2\pi h \times \int_0^R \varepsilon_0\varepsilon_3|E_0|^2 \cdot e^{-(R-r)/L} r dr}{\int \varepsilon_0\varepsilon(r) \cdot |E(r)|^2 dV} \approx \frac{2\pi R h \times \varepsilon_0 n_3^2 |E_0|^2 L}{\int \varepsilon_0\varepsilon(r) \cdot |E(r)|^2 dV} \qquad (4)$$

where E_0 is the electric field at ring resonator inner surface and h is an arbitrary length along ring resonator longitudinal direction. Specially, Eq. (3) is also valid when η_3 equal to 0 or 1. The light intensity decay constant is L which is given by:

$$L = \frac{\lambda}{4\pi\sqrt{n_2^2 - n_3^2}} \qquad (5)$$

Therefore, in order to intuitively analyze sensitivity, based on Eqs. (2)–(5), the sensitivity S of sensor is given by [36]:

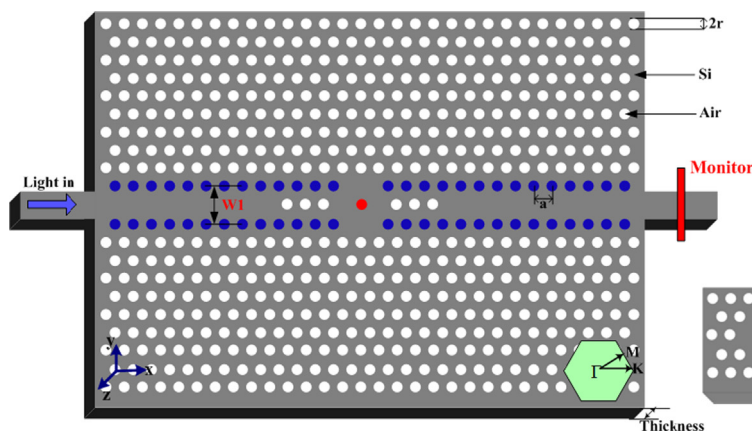$$S = \frac{\Delta\lambda}{\Delta n} = \frac{\lambda}{n_2} \cdot \eta_3 \qquad (6)$$

Fig. 4. The 3D illustration of a sensing element in the RDCR structure, where $a=348$ nm, $r=0.34a$, $T=0.55a$.
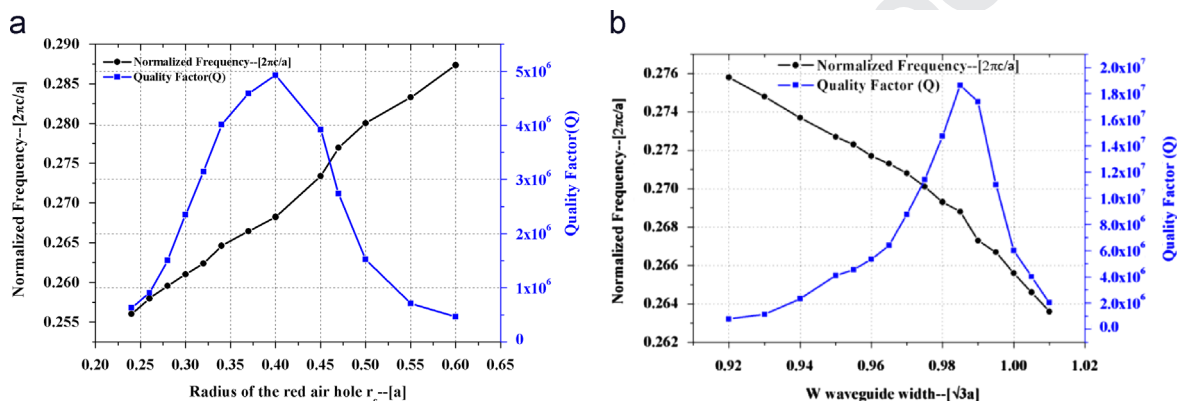

Fig. 5. (a) Results of 3D-FDTD calculations showing resonance frequencies and Q factors as a function of radius of the red air holes r_c in the ring resonator. (b) Results of 3D-FDTD calculations showing resonance frequencies and Q factors as a function of line defect waveguide width W when $r_c=0.40a$. (For interpretation of the references to color in this figure legend, the reader is referred to the web version of this article.)
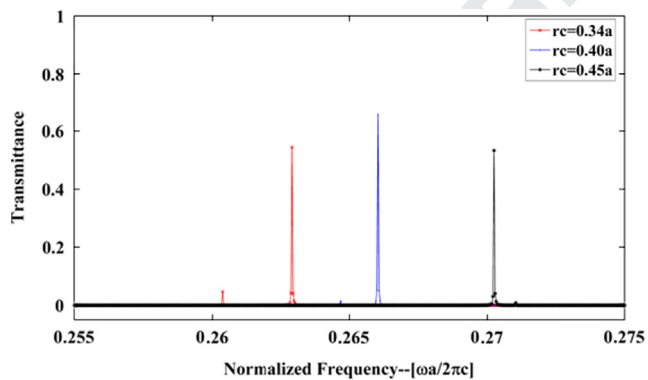

Fig. 6. The transmission spectra of TE-like polarized lightwave with different parameters $r_c=0.34a$, $0.40a$ and $0.45a$.
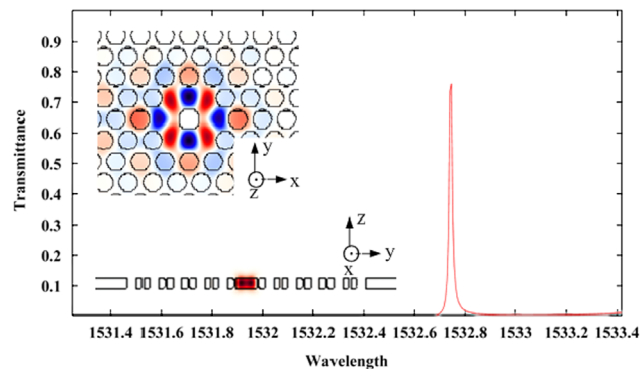

Fig. 7. The transmission spectrum of TE-like polarized profile light-wave when $r_c=0.40a$, $W=0.99W_1$. The inset shows the electric field profile for the fundamental quasi-TE mode.

We here employ detailed 3D-FDTD simulations that permit us to analysis the sensitivity of this sensor and how to obtain lowest mass limit of detection. We assume that molecules in glycerol solution are infiltrated into air holes around the resonant cavity area, thus the specific capture of glycerol solution molecules at the sensor surface results in a local change in RI, inducing a sensing signal that enables good quantification of the biomolecules in the sensor.

4.2. Simulate calculations

4.2.1. Sensitivity of one hole inner ring resonator

In this paper, as shown in Fig. 7, there is a significant amount of light confined within the ring resonator. Considering the evanescent field at side wall of the ring resonator, most of the surrounding holes of ring resonator should have a stronger optical field. This situation makes the resonator to be more sensitivity to refractive index changes within these holes due to large degree of light-matter interaction. Therefore, we alter the number of holes ($N=N_{in}+N_s$) being functionalized to analyze the mass sensitivity S_m ($S_m=\Delta\lambda/N$), which is defined as a function of the number of functionalized holes. Where N_{in} represents the number of air holes inner ring resonator, and N_s is the number of air holes surrounding the ring resonator. Simulations are performed in Fig. 9(c) with one hole, 13 holes, 31 holes, 55 holes, and up to 83 holes. The mass sensitivity ($S_m=\Delta\lambda/N$) as a function of N is shown in Fig. 9(a), and the wavelength shift ($\Delta\lambda$) as a function of N is shown in Fig. 9(b), where $\Delta\lambda$ is the shift in the resonant wavelength
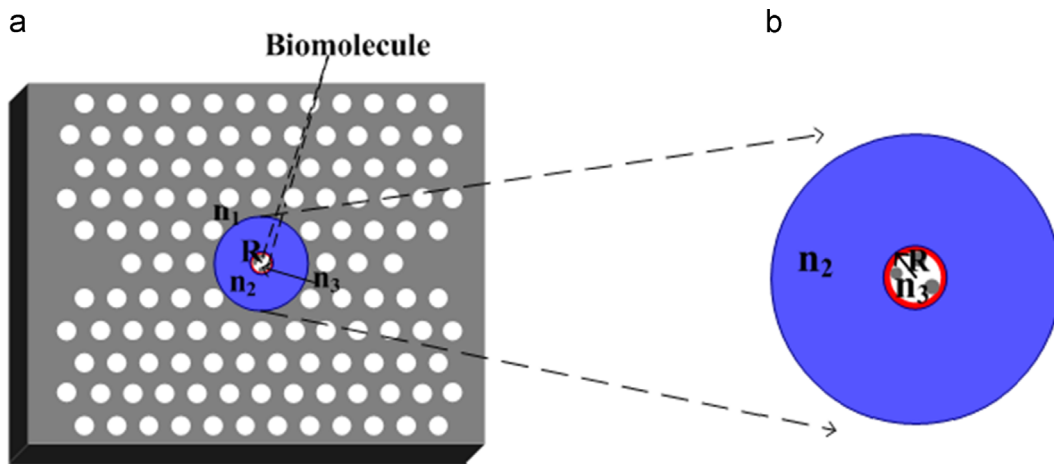
Fig. 8. (a) The structure illustration of ring resonator, $\varepsilon_1=n_1^2$, $\varepsilon_2=n_2^2$ and $\varepsilon_3=n_3^2$ representing dielectric constant for surrounding medium, wall, and core. R is the effective inner radius of ring resonator. (b) The amplified image of ring resonator in (a).
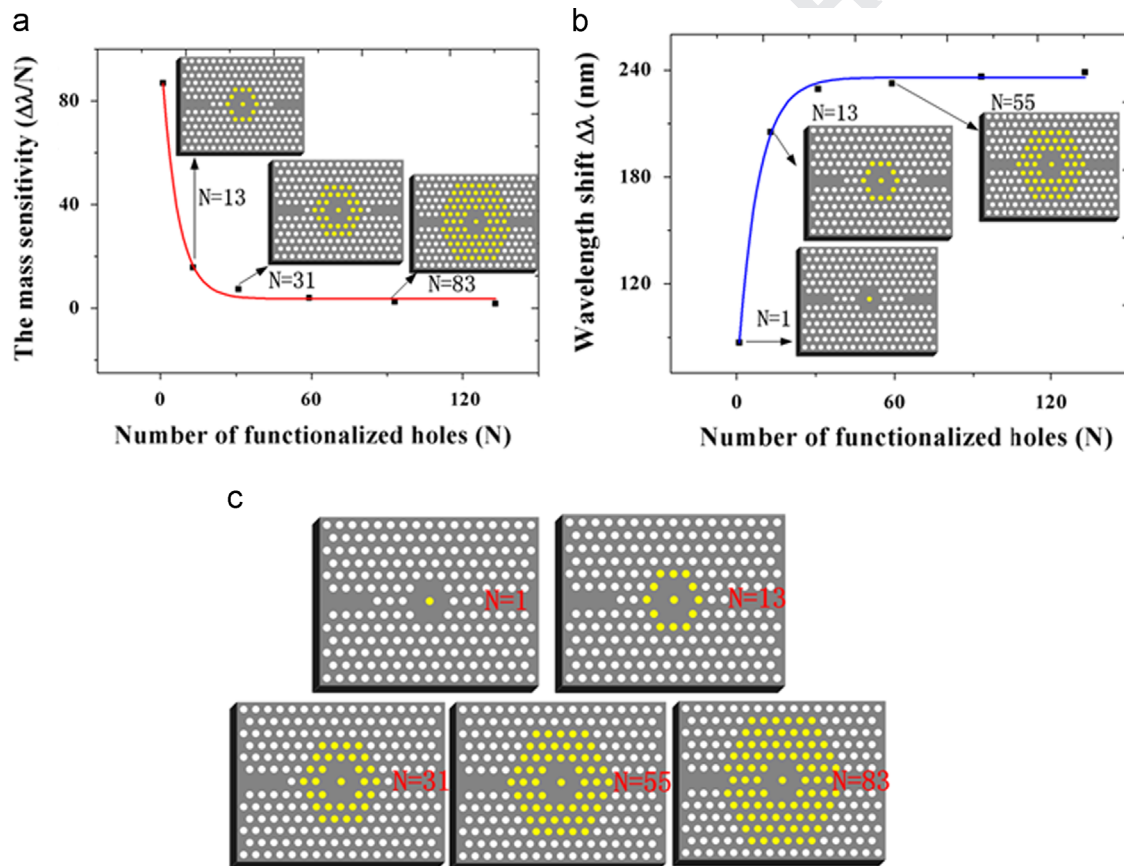

Fig. 9. (a) The mass sensitivity as a function of the number of functionalized holes. The blank squares indicate values of the mass sensitivity calculated from 3D-FDTD simulations. The red curve shows an exponential fit of the form $a+b\cdot e^{-N/c}$, where a, b and c are arbitrary constants. The values a, b and c are equal to 3.6349, 97.442 and 6.35, respectively, and the regression coefficient equal to 0.9958. The inset shows the schematic illustration of number of functionalized holes $N=13$, 31, and 83. (b) Plot illustrating the dependence of the shift resonant wavelength and the number of functionalized holes. The blue curve is a best-fit curve of the form $a+be^{-N/c}$. The values of a, b, c used here are 236, -169.5195 and 7.7364, respectively, and the regression coefficient is 0.9945. The inset shows the schematic illustration of number of functionalized holes $N=1$, 13, and 55. The functionalized holes number ($N=N_{in}+N_s$), N_{in} represents the number of air hole inner ring resonator, and N_s is the number of air holes surrounding the ring resonator. (c) Based on the number $N_{in}=1$, simulations are performed for the cases with one hole, 13 holes, 31 holes, 55 holes, 83 holes. (For interpretation of the references to color in this figure legend, the reader is referred to the web version of this article.)

and N is the number of functionalized holes. In Fig. 9(a), the values of calculated S_m are marked out with black squares, as expected all along, and the values are decreased exponentially with the increase of number (N) of functionalized holes, which show the center hole inner ring resonator responding to most sensitive to any refractive index changes as opposed to the air holes that are further away from ring resonant cavity. These results can also be explained by noticing that the evanescent field in Fig. 7. This is very important to notice that targeting only the center hole for functionalization allows lowest possible limit of mass detection.
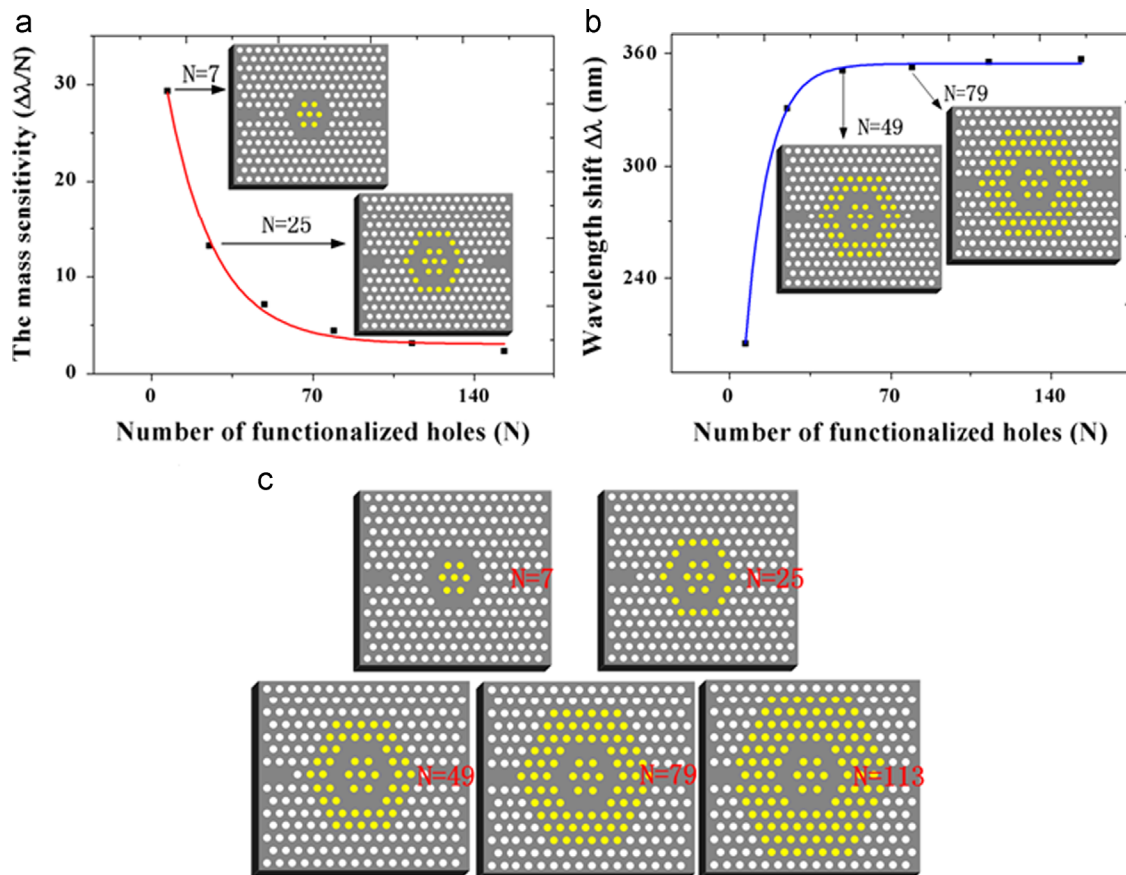
Fig. 10. (a) The mass sensitivity as a function of the number of functionalized holes. The red curve is a best-fit curve of the form $a + b \cdot e^{-N/c}$, where the values of a, b and c are 3.0675, 36.7229 and 20.5076, respectively, and the regression coefficient is 0.9937. The inset shows the schematic illustration of number of functionalized holes $N=7$, 25. (b) The relation of the shift resonant wavelength and the number of functionalized holes. The blue curve is a best-fit curve of the form $a + b \cdot e^{-N/c}$, where the values of a, b and c used here are 354.4379, -303.1445 and 9.8639, respectively, and the regression coefficient is 0.9988. The inset shows the schematic illustration of number of functionalized holes $N=49$, 79. (c) Based on the number $N_{in}=7$, simulations are performed with 7 holes, 25 holes, 49 holes, 79 holes and up to 113 holes. (For interpretation of the references to color in this figure legend, the reader is referred to the web version of this article.)
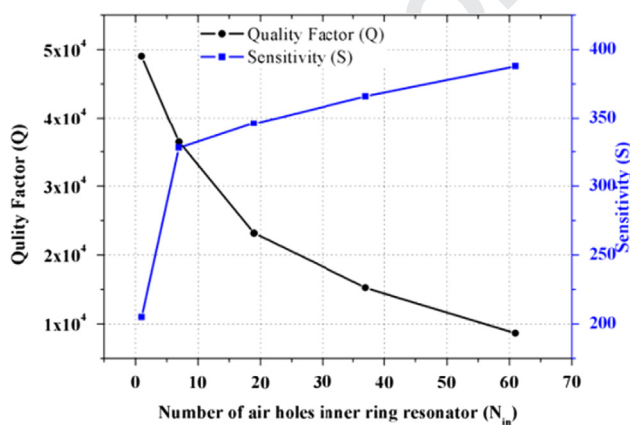

Fig. 11. The Q factor and S as a function of N_{in} inner ring resonator with water absorption and random roughness of fabrication.

We notice that an exponential function fitting the black squares in Fig. 9(a) can be expressed by [20]:

$$\frac{\Delta\lambda}{N} = a + b \cdot e^{-\frac{N}{c}} \tag{7}$$

where a, b and c are arbitrary constant parameters. The values a, b and c are equal to 3.6349, 97.442 and 6.35, respectively, and the regression coefficient equals to 0.9958. This shows that the analytical express shows quite good agreement with the 3D-

FDTD simulation results and explains well that how the mass sensitivity varies with the variation of the functionalized holes. Based on the Eq. (7), we can enhance the mass sensitivity of the sample when we decrease the number of the functionalized air holes. Similarly, Eq. (7) can also exponential fitting the black squares in Fig. 9(b), and the values a, b and c are equal to 236, -169.5195 and 7.7364, respectively, and the regression coefficient is 0.9945. As shown in Fig. 9(b), the wavelength shift $\Delta\lambda$ is larger when the functionalized holes increase and a demarcation point $N=13$ can be seen. In the left of $N=13$, the mass sensitivity ($S_m = \Delta\lambda/N$) is higher, whereas the sensitivity ($S = \Delta\lambda/\Delta n$) is lower. Similarly, in the right of $N=13$, we can implement higher sensitivity, but the mass sensitivity is lower. Therefore, we make a tradeoff between the refractive index sensitivity and the mass sensitivity and determine the functionalized air holes $N=13$, namely, we alter the refractive index of the center and one round functionalized holes near the ring resonator to obtain a tradeoff between the refractive index sensitivity and the mass sensitivity.

4.2.2. Sensitivity of multiple holes inner ring resonator

Based on the above discussion, in view of possessing higher sensitivity of air holes inner ring resonator, we change the structure and adjust the radius of the ring resonance cavity (namely, it can contains the number of holes (N_{in})). We therefore increase the number of the air holes inner the ring resonator by adding one round ($N_{in}=7$ holes). The S_m as a function of the functionalized holes (N) inner ring resonator is shown in Fig. 10(a),

and the $\Delta\lambda$ as a function of the functionalized holes (N) is shown in Fig. 10(b). Simulations are performed in Fig. 10(c) with 7 holes, 25 holes, 49 holes, 79 holes, 113 holes. As shown in Fig. 10(b), the wavelength shift $\Delta\lambda$ is larger and a demarcation point $N=25$ can be seen when the number of functionalized holes is increased. In the left of $N=25$, the mass sensitivity S_m is higher, whereas the sensitivity S is lower. However, in the right of $N=25$, the mass sensitivity S_m is lower, but the sensitivity S is higher. Therefore, we alter 25 functionalized holes in this situation to obtain optimal properties when we consider the complexity of fabrication and the tradeoff of the sensitivity S and the mass sensitivity S_m.

4.2.3. The discussion of optimal FOM by adjusting the number N_{in}

We increase air holes (N_{in}) again inner ring resonator round and round according to the above steps, namely, by adding two round (19 holes), three round (37 holes), four round (61 holes), respectively. The optimal Q factor and sensitivity with water absorption and random roughness of fabrication as a function of N_{in} inner ring resonator in different structures are shown in Fig. 11. As shown in Fig. 11, the sensitivity is enhanced with increasing of N_{in} inner ring resonator, whereas the Q factor is declined. Therefore, we choose a tradeoff between Q factor and sensitivity, the maximum product of Q factor and sensitivity can be obtained when the number N_{in} equal to 7 inner ring resonator, resulting in optimal FOM.

5. Ring defect coupled resonator design and simulation results

Through the discussion about high Q factor and sensitivity S, the label-free biochemical sensor is made up of $N_{in}=7$ air holes inner the ring resonator. Fig. 12(a) and (b) shows the 3D schematic view of the RDCR structure and fundamental quasi-TE mode through ring defect coupled resonator, respectively. The results of numerical simulations show that the total Q factor is about 8.2×10^6 and resonant wavelength is at near 1500 nm obtained from 3D-FDTD simulation. In addition, we also consider the effect of fabrication roughness (e.g., random roughness) in our sample when water absorption is considered. The simulation was performed in a water environment (neglecting water absorption), assuming a change of the air holes of roughness from 0 to 5, 0 to 10, 0 to 15, and 0 to 20 nm. The Q factor as a function of roughness of the air holes is shown in Fig. 13. We can obtain minimum $Q=35,517$ when the random roughness of air holes is about 20 nm. In order to quantitatively well analyze RI sensitivity of the sensor, we here alter the refractive index with $n=1.315$, 1.330 and 1.345 corresponding to deuterium water ($n_{1.330}$) and glycerol solutions ($n_{1.345}$), and the transmission of TE-like polarized light-wave with different parameters of refractive index as a function of wavelength is shown in Fig. 14.
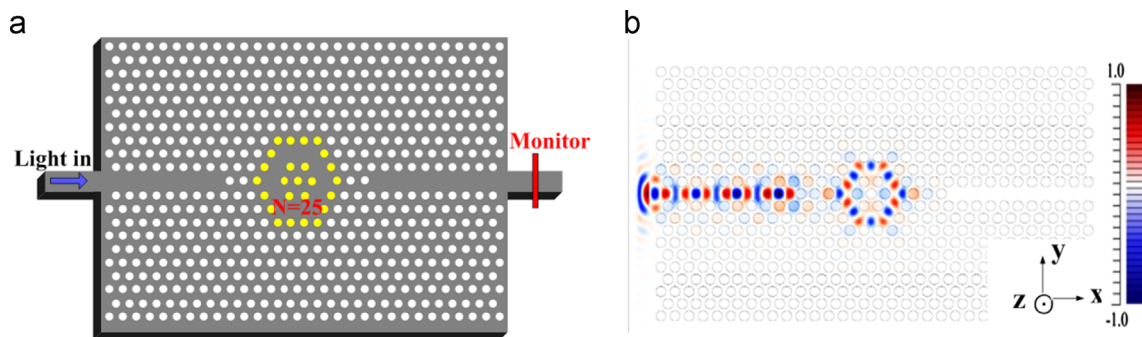
From the simulation results shown in Fig. 14, taking water absorption and random roughness of fabrication into consideration at telecom wavelength range, the sensitivity is equal to 330 nm/RIU. In order to analyze quantitatively sensing of glycerol solution, the sensitivity (S) and the resolution (R_0) combine to calculate the detection limit (DL) of the sample giving by [37]

$$DL = \frac{R_0}{S} \tag{8}$$

where the DL describes the minimum amount of glycerol molecule that the sensor can accurately quantify, and the sensor resolution characterizes the smallest possible spectral shift that can be accurately measured. Here we can assume a minimal resolvable wavelength shift to a linewidth R_0 giving by [21,37]:

$$R_0 = \frac{\lambda_0}{10 \cdot Q} \tag{9}$$

where λ_0 and Q are the wavelength and quality factor of the resonance peak, respectively. We calculate the minimal resolvable detectable change $DL=1.24 \times 10^{-5}$. Besides, compared with the techniques like SPR, the ability to drastically confine the detection volume by targeting the inner most air holes in our sample allows us to lower the mass limit of detection. The figure of merit (FOM) of the sensor can be define as [3,26,30,31]:

$$FOM = S \cdot Q / \lambda_0 \tag{10}$$

Based on the Eq. (10), we obtain the figure of merit FOM of 8000. This is, to the best of our knowledge, the first photonic
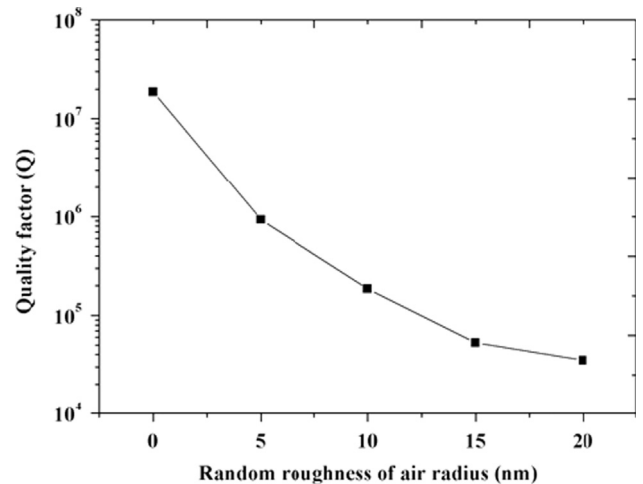
Fig. 13. The Q factors of the sample with change of random roughness from 0 to 5, 0 to 10, 0 to 15, and 0 to 20 nm.

Fig. 12. (a) Schematic view of ring defect coupled resonator structure. Under the yellow shaded area there are 25 functionalized holes ($N=25$). (b) The electric field profile for fundamental quasi-TE mode through ring resonator in x–y plane. (For interpretation of the references to color in this figure legend, the reader is referred to the web version of this article.)
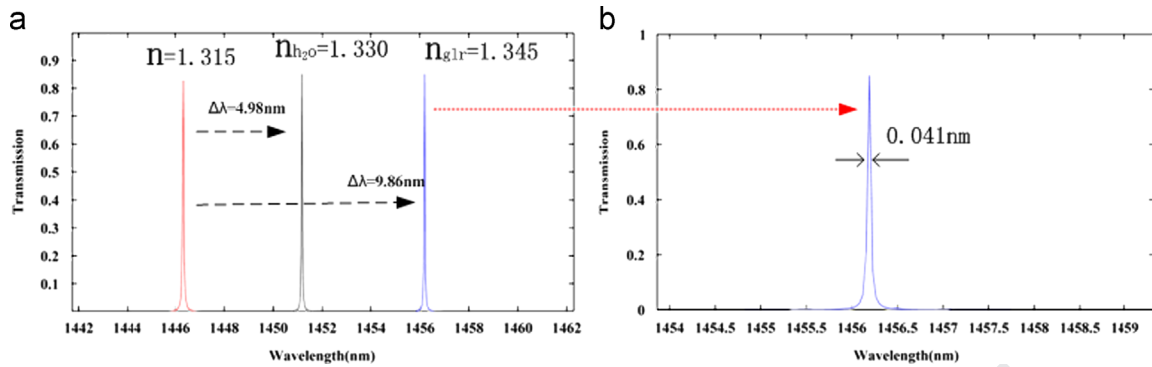
Fig. 14. (a) The transmission of TE-like polarized light-wave with different refractive index parameters as a function of wavelength.(b) The amplified image of the blue transmission peak in (a). (For interpretation of the references to color in this figure legend, the reader is referred to the web version of this article.)

crystal structures that have simultaneously high Q and S and supply an ideal platform for biochemical sensing.

6. Conclusion

In this paper, we have designed a novel ring defect coupled resonator, which has been characterized by the structure adjustment and simulations. The sample consists of a ring resonator cavity and line defect waveguide with high Q factor and sensitivity. The resonant cavity results in a shift in the resonant wavelength when we alter the refractive index of surrounding air holes by the RI of deuterium water and glycerol solution. According to the simulation results, we have achieved high Q of 10^7. Even though the simulation considers the random roughness of fabrication of the air holes and water absorption at telecom wavelength range, the Q factor can achieve 35,517 and the sensitivity can be enhanced to 330 nm/RIU simultaneously, resulting in *FOM* of $\sim$8000. Moreover, this sample can also detect a minimal change as good as $DL = 1.24 \times 10^{-5}$. Therefore, this sensor is a potentially ideal platform for refractive index-based medical diagnoses and life sciences.

Acknowledgments

References

[1] J. Homola, S. Yee, G. Gauglitz, Sens, Actuators B: Chem. 54 (1999) 3.
[2] J.N. Anker, W.P. Hall, O. Lyandres, N.C. Shah, J. Zhao, R.P. Duyne, Nat. Mater. 7 (2008) 442.
[3] Y. Shen, J. Zhou, T. Liu, Y. Tao, R. Jiang, M. Liu, G. Xiao, J. Zhu, Z. Zhou, X. Wang, C. Jin, J. Wang, Nat. Commun. 4 (2013) 2381.
[4] L. Rindorf, J.B. Jensen, H.M. Dufva, L.H. Pedersen, P.E. Hoiby, O. Bang, Opt. Express 14 (2006) 8224.
[5] Niels Asger Mortensen, Sanshui Xiao, Jesper Pedersen, Microfluid. Nanofluid. 4 (1-2) (2008) 117.
[6] C.Y. Chao, L.J. Guo, Appl. Phys. Lett. 83 (2003) 1527.
[7] A. Ksendzov, Y. Lin, Opt. Lett. 30 (2005) 3344.
[8] C.Y. Chao, W. Fung, L.J. Guo, IEEE J. Sel. Top. Quantum Electron. 12 (2006) 134.
[9] A. Yalcin, K.C. Popat, O.C. Aldridge, T.A. Desai, J. Hryniewicz, N. Chbouki, B.E. Little, O. King, V. Van, S. Chu, D. Gill, M. Anthes-Washburn, M.S. Unlu, B.B. Goldberg, IEEE J. Sel. Top. Quantum Electron. 12 (2006) 148.
[10] H. Zhu, I.M. White, J.D. Suter, P.S. Dale, X. Fan, Opt. Express 15 (2007) 9139.
[11] C.A. Barrios, K.B. Gylfason, B. Snchez, A. Griol, H. Sohlstrm, M. Holgado, R. Casquel, Opt. Lett. 32 (2007) 3080.
[12] T. Claes, J.G. Molera, K. De Vos, E. Schacht, R. Baets, P. Bienstman, IEEE Photonics J. 1 (2009) 197.
[13] G.D. Kim, G.S. Son, H.S. Lee, K.D. Kim, S.S. Lee, Opt. Commun. 281 (2008) 4644.
[14] T. Ling, L.J. Guo, Opt. Express 15 (2007) 17424.
[15] V. Zamora, A. Díez, M.V. Andrés, B. Gimeno, Opt. Express 15 (2007) 12011.
[16] T. Ling, L.J. Guo, Appl. Phys. Lett. 103 (2013) 013702.
[17] Q. Quan, F. Vollmer, I.B. Burgess, P.B. Deotare, I.W. Frank, T. Sindy, K.Y. Tang, R. Illic, and M. Loncar, in: Proc. 2011 Quantum Electronics and Laser Science Conference (QELS), Baltimore, Maryland, 1 May, 2011.
[18] E. Kuramochi, M. Notomi, S. Mitsugi, A. Shinya, T. Tanabe, Appl. Phys. Lett. 88 (2006) 041112.
[19] X. Wang, Z. Xu, N. Lu, J. Zhu, G. Jin, Opt. Commun. 281 (2008) 1725.
[20] D. Yang, H. Tian, Y. Ji, Opt. Express 19 (2011) 20023.
[21] D. Dorfner, T. Zabel, T. Hürlimann, N. Hauke, L. Frandsen, G. Abstreiter, J. Finley, Biosens. Bioelectron. 24 (2009) 3688.
[22] T. Xu, N. Zhu, M.Y. Xu, L. Wosinski, J.S. Aitchison, H.E. Ruda, Opt. Express 18 (2010) 5420.
[23] D. Yang, H. Tian, Y. Ji, Opt. Commun. 284 (2011) 4986.
[24] Shota Kita, Shoji Hachuda, Shota Otsuka, Tatsuro Endo, Yasunori Imai, Yoshiaki Nishijima, Hiroaki Misawa, Toshihiko Baba, Opt. Express 19 (2011) 17683.
[25] B. Wang, M.A. Dündar, R. Nötzel, F. Karouta, S. He, R.W van der Heijden, Proc. SPIE 7946 (2011) 79461C.
[26] D. Yang, H. Tian, Y. Ji, Q. Quan, J. Opt. Soc. Am. B 30 (2013) 2027.
[27] S.H. Kwon, T. Sünner, M. Kamp, A. Forchel, Opt. Express 16 (2008) 11709.
[28] K.V. Sreekanth, S. Zeng, K.-T. Yong, T. Yu, Sens. Actuators B: Chem. 182 (2013) 424.
[29] S. Hachuda, S. Otsuka, S. Kita, T. Isono, M. Narimatsu, K. Watanabe, Y. Goshima, T. Baba, Opt. Express 21 (2013) 12815.
[30] A. Sinibaldi, R. Rizzo, G. Figliozzi, E. Descrovi, N. Danz, P. Munzert, A. Anopchenko, F. Michelotti, Opt. Express 21 (2013) 23331.
[31] A. Sinibaldi, N. Danz, E. Descrovi, P. Munzert, U. Schulz, F. Sonntag, L. Dominici, F. Michelotti, Sens. Actuators B: Chem. 174 (2012) 292.
[32] M. Notomi, E. Kuramochi, T. Tanabe, Nat. Photon 2 (2008) 741.
[33] B.S. Song, S. Noda, T. Asano, Y. Akahane, Nat. Mater. 4 (2005) 207.
[34] S.H. Kwon, T. Sünner, M. Kamp, A. Forchel, Opt. Express 16 (2008) 4605.
[35] Q. Quan, M. Lončar, Opt. Express 19 (2011) 18529.
[36] S. Arnold, M. Khoshsima, I. Teraoka, S. Holler, F. Vollmer, Opt. Lett. 28 (2003) 272.
[37] Ian M. White, X. Fan, Opt. Express 16 (2008) 1020.